Comparison of damaging behavior of oxide scales grown on austenitic stainless steels using tensile test and cyclic thermogravimetry

E. Fedorova [a,b], M. Braccini [c,d], V. Parry [c,d], C. Pascal [c,d], M. Mantel [c,d,e], F. Roussel-Dherbey [f], D. Oquab [b], Y. Wouters [c,d], D. Monceau [b,*]

[a] Polytechnic Institute of Siberian Federal University, Krasnoyarsk, Russia
[b] U. Toulouse, Institut Carnot CIRIMAT, ENSIACET, F-31030 France
[c] U. Grenoble Alpes, SIMAP, F-38000 Grenoble, France
[d] CNRS, SIMAP, F-38000 Grenoble, France
[e] UGITECH SA, Ugine, France
[f] U. Grenoble Alpes, CMTC, F-38000 Grenoble, France

A B S T R A C T

Two austenitic stainless steels, AISI 304L and AISI 303, were submitted to cyclic oxidation and to static mechanical loading after isothermal oxidation at 1000 °C. Alloy 303 contains ten times more S than 304L and some Mn addition. During the steel process, it formed manganese sulfides that lead to the formation of a less resistant oxide scale. Both alloys showed similar behavior during thermal cycling but breakaway oxidation and intensive spallation occurred much sooner for alloy 303 than for alloy 304L. A correlation could be drawn between tensile test on preoxidized samples, isothermal and cyclic oxidation.

Keywords:
Stainless steel
Thermal cycling
Oxidation
Interfaces
Sulfur

1. Introduction

Maintaining good adhesion of the protective oxide layer on the surface of heat-resistant alloys is crucial for long-term cyclic oxidation resistance. Negative effect of S on the adherence of oxide scales grown on alumina or chromia forming alloys after high temperature isothermal or cyclic oxidation have been widely studied and are known to be a major cause of protective layer failure [1–5]. It was shown that S segregates to free surfaces of voids and cavities formed beneath the oxide scale, further promoting the weakening and consequently the delamination of the metal/oxide interface [6]. On the other hand, calculations and experimental investigations demonstrated the presence of S segregations also at intact interfaces [4,7] and at oxide grain boundaries, which affects the oxide growth mechanism [8]. For chromia scales, the prevailing effect of scale failure appeared to be the interfacial morphology associated with growth stresses, whereas S segregation at the interface is only a secondary effect [1,8].

Most industrial stainless steels contain S to improve steel machinability. S is considered as a detrimental element not only for oxide layer adhesion but also for hot ductility which is essential for forging and rolling. Therefore Mn is added in steels to avoid iron sulfide formation (FeS) which are non-deformable harmful inclusions. S is then trapped by Mn and precipitates as Mn sulfides in the liquid state and during solidification. These inclusions exhibit a lower hardness than Fe sulfides at high temperature and are elongated during hot rolling. At high temperature, the equilibrium between S in sulfides and S in solid solution in the Fe–Ni–Cr matrix is established, this controls the concentration of “free” S. During the high temperature oxidation of steels, oxidation of Mn sulfides can also free some additional S which can diffuse to the metal surface. This can change the metal/oxide interfacial behavior and decrease the adherence of the growing oxide layer. A more subtle mechanism was recently proposed in a companion paper [9]. Indeed, it was shown that when MnS precipitates are oxidized, some S is released and reacts with Cr to form Cr oxysulfides. Therefore the quantity of Cr available for the formation of a protective chromia scale becomes insufficient. Consequently, an accelerated

* Corresponding author at: CIRIMAT Laboratory, University of Toulouse, ENSIACET 4, allée Emile Monso, BP-44362, 31030 Toulouse Cedex 4, France. Fax: +33 534323422.
E-mail address: Daniel.monceau@ensiacet.fr (D. Monceau).

http://dx.doi.org/10.1016/j.corsci.2015.11.012

Table 1
Chemical composition of austenitic stainless steels AISI 304L and AISI 303 (wt.%).

Steel	Ni	Cr	Mn	Mo	Si	C	S	N	O	Ca
AISI 304L	8.96	18.0	1.13	0.40	0.46	0.021	0.025	0.048	0.010	0.005
AISI 303	8.28	17.1	1.75	0.40	0.44	0.055	0.295	0.035	0.015	0.013

oxidation of the depleted alloy occurs (breakaway), leading to an oxide scale with poor mechanical properties.

To predict oxide scale lifetime before spallation, it is necessary to know the oxide/metal interface adhesion and the oxide scale mechanical behavior. The methods used to measure them are similar to the ones developed for brittle film on ductile substrate. Some of them are very simple to perform because they do not require any sample preparation, like indentation [10] or scratch test [11–13]. Nevertheless, those methods often lead to semi-quantitative information. Moreover, the oxide surface roughness can be an issue. Other methods called "sandwich specimen" methods, such as 4-point bending tests [14] for example, lead to more accurate measurements of the oxide/metal adhesion but they require more sample processing. In particular, a dummy substrate has to be glued onto the surface of the oxide. This bonding can become prohibitive: sometimes no measurement can be obtained because decohesion occurs in the adhesive bond instead of the oxide/metal interface. Finally, some adhesion measurements consist in imposing uniaxial tensile strain on the oxide film while observing the oxide surface with a microscope [15,16]. During such in situ SEM, mechanical tests the oxide scale can exhibit transverse cracks and/or spallation areas. Based on the quantification of those damages, the mechanical properties of the oxide scale such as toughness and adhesion, can be evaluated [17,18]. Nevertheless, like in all the other techniques described here, the knowledge of the residual stress in the oxide scale due to its growth is needed to accurately quantify those properties [19].

It was shown that cyclic continuous thermogravimetry analysis (CTGA) is a fast way to obtain an evaluation of the material resistance to cyclic oxidation and to compare the performance of different materials [20]. This technique combines the assessment of the oxidation kinetics and the assessment of the resistance to thermal cycling with associated stresses. It is therefore interesting to try to correlate CTGA results with isothermal oxidation kinetics as well as with the evaluation of the mechanical properties of the oxide/metal system. The main objective of the present study is to investigate the oxide/metal interfacial behavior during high temperature cyclic oxidation of austenitic stainless steels in relation with the static mechanical loading of pre-oxidized samples. The S content is used as a sensitive parameter influencing the growth kinetics and mechanical resistance of the oxide scale.

2. Experimental procedure

2.1. Materials and methods

Two austenitic stainless steels AISI 304L and AISI 303 provided by Ugitech were chosen as substrates. The alloys were produced by continuous casting and bars of 20 mm were made by hot rolling. These bars were then cold drawn with a 15% reduction of the section. The chemical composition of the investigated materials was controlled by Fluorescence Spectroscopy Analysis and Optical Emission Spectrometry equipped with a gas analyzer. The amount of minor elements in both steels was controlled to make sure their concentrations were similar. They were, except for S and Mn. AISI 304L contains 0.025 wt.% of S and 1.13 wt.% of Mn, whereas the AISI 303 steel contains 0.295 wt.% S and 1.75 wt.% Mn. A difference in carbon content can be noticed, with a higher concentration for alloy 303. Alloys compositions are given in Table 1.

In order to characterize the microstructure prior to oxidation testing, optical microscopy has been performed on the cross section of the samples. Samples have been electrolytically etched in an 85% nitric acid solution for 10 s at 20 mA cm^{-2} to reveal manganese sulfides MnS (in black in Fig. 1b, d) and residual δ-ferrite (in grey in Fig. 1b, d). They were etched in the same solution for 40 s at 20 mA cm^{-2} to reveal grain size (Fig. 1a, c). For AISI 304L, the mean grain size is around 30 μm, and around 22 μm for AISI 303. The main difference between the two microstructures lies in the presence of numerous inclusions of MnS in the AISI 303 due to its higher S content. After etching, Mn sulfides appear in black in Fig. 1. As these inclusions are highly deformable at rolling process temperatures, they also indicate the longitudinal axis of the sample. As the solidification starts in the δ-ferrite phase, we also observe some residual ferrite that has not transformed into austenite during solidification. These ferrite islands have also been deformed during hot rolling. AISI 304L shows slightly more ferrite (~2%) than AISI 303 (~1%) as a direct consequence of the chemical composition of the two grades.

2.2. Samples preparation

Specimens were obtained from 22 to 24 mm diameter rods. Rectangular plates were cut in the longitudinal direction by electrical discharge machining. Parallelepipedic samples with dimensions of 17 mm × 10 mm × 2 mm (Fig. 2) were machined for thermogravimetric tests. Prior to oxidation, all sides of the specimens were ground with SiC paper, down to a final grade of P1200. All samples were cleaned in an ultrasonic bath with acetone followed by high-purity alcohol. They were weighed with an accuracy to within 10 μg with a Sartorius ME balance before and after high-temperature exposures.

Flat specimens for in situ SEM tensile tests were machined from rectangular 1 mm thick plates using electrical discharge machining. Fig. 2 shows the specimen geometry presenting a gauge section of 2 mm width by 1 mm thick and a gauge length of 3 mm. Prior to oxidation, the tensile specimens underwent the same preparation route as TG samples.

2.3. Experimental conditions

Tensile specimens were isothermally oxidized in a tubular furnace at 1000 °C with a heating rate of 60 °C min^{-1}. Synthetic air flow rate was maintained at 0.6 l h^{-1} corresponding to a linear flow rate of 0.17 cm s^{-1} at RT.

Cyclic thermogravimetry analysis (CTGA) was applied to the cyclic oxidation at 1000 °C on the same thermobalance than for the isothermal thermogravimetry. A commercial SETARAM™ TAG 24S thermobalance ensuring a sensitivity better than 1 μg was used. The device has a double symmetrical furnace designed to compensate signal disturbances resulting from gas flow, buoyancy and convection. It is suitable for the accurate measurement of small mass variations occurring during short oxidation tests or induced by very slow-growing oxide scale such as alumina and chromia scales. Through air flow modulation during a dummy isothermal experiment, it was checked that the chosen synthetic air flow rate was sufficient to leave the oxidation kinetics unaffected. CTGA not only allowed the assessment of oxidation kinetics but also the measurement of any oxide scale spallation occurring during specimen

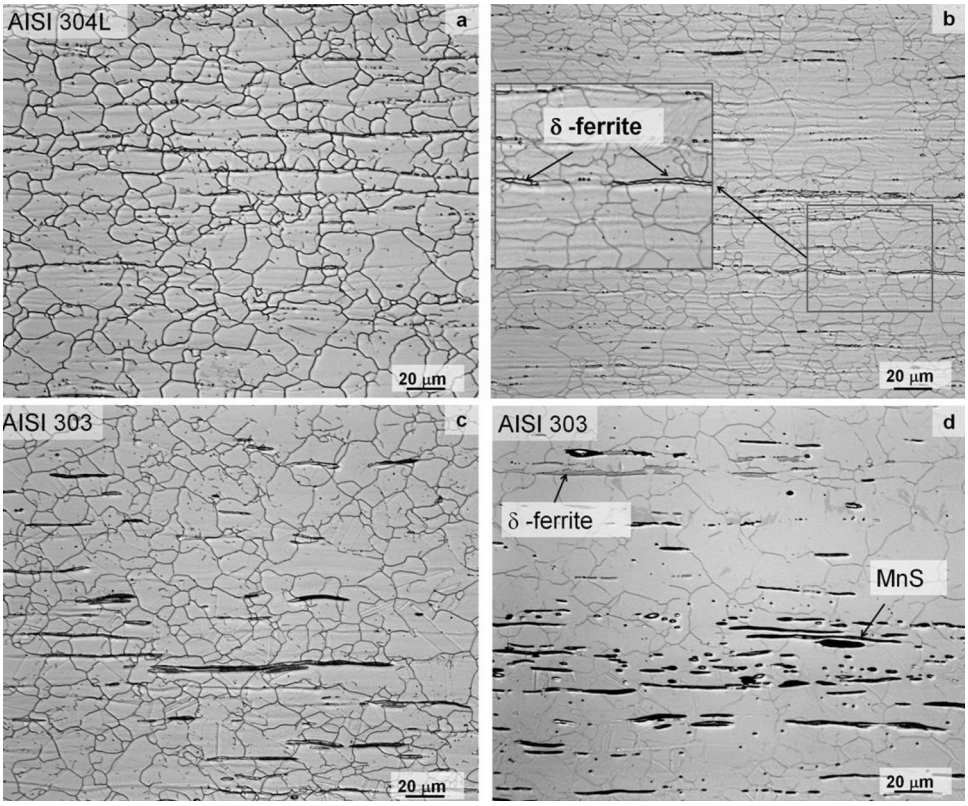

Fig. 1. Microstructures of the AISI 304L (a, b) and AISI 303 (c, d) in the as-received condition (horizontal = direction of rolling i.e. longitudinal axis of the sample).

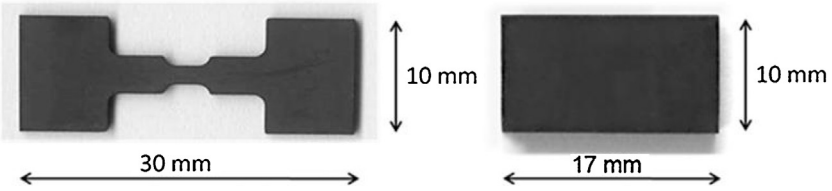

Fig. 2. Geometry of in situ tensile and CTGA test specimens.

heating or cooling. The thermal cycle consisted of a heating period of 60 °C min^{-1} up to 1000 °C, followed by a dwell of 60 min at 1000 °C and a cooling ramp with an initial rate of 60 °C min^{-1}. The total duration of one cycle was 180 min. This experiment was carried out under flowing synthetic air at the same flow rate used for isothermal oxidation.

Pre-oxidized tensile specimens were loaded into a homemade micromechanical device adapted into a JEOL JSM 6400 scanning electron microscope. This device permits the continuous observation at a microscopic scale of the damage mechanisms in the oxide layer. The straining system induces a symmetrical displacement of the grips so the observation of the sample surface does not require refocusing nor recovery of the observation area. A displacement rate of 100 μm min^{-1} was chosen. During one tensile test, the uniform central part of the sample was carefully observed. The displacement motion was interrupted in order to acquire images of the sample surface. Sequential micrographs of the evolution of the damage in the oxide layers have been collected according to the applied strain.

The oxidized samples were cross-sectioned and prepared for metallographic analysis using conventional techniques, i.e. grinding, polishing and fine polishing. Prior to mounting, the samples were coated with a thin epoxy resin layer to protect the oxide scale. The morphology and microstructure of the oxide scales formed on steels was characterized using optical metallography, scanning electron microscopy (SEM) on a LEO 435VP system as well as on FEG SEM 7001F JEOL coupled with electron backscatter diffraction system (EBSD). The chemical analysis by means of a PGT (imix-PC) system for the EDS with real standards was performed as a complementary study.

The oxide and substrate phase structures were identified by X-ray diffraction (XRD) using a Seifert 3000TT and D8 Advance diffractometers CuKα radiation. These characterizations were completed by Raman spectroscopy using a Renishaw RM1000 Raman microscope.

3. Results and discussions

3.1. Corrosion behavior under isothermal oxidation

Isothermal oxidation kinetics at 1000 °C were already reported in [9]. It was shown that some variations in mass gain occurred during the oxidation process. Nevertheless, the calculation of the parabolic constant calculated after the transient regime, using the complete parabolic law [21], allowed to conclude that the isothermal oxidation kinetics of alloy 303 were, in average, 5 times faster than the oxidation kinetics of alloy 304L. Indeed, the parabolic constant after transient regime was between 1.1×10^{-5}

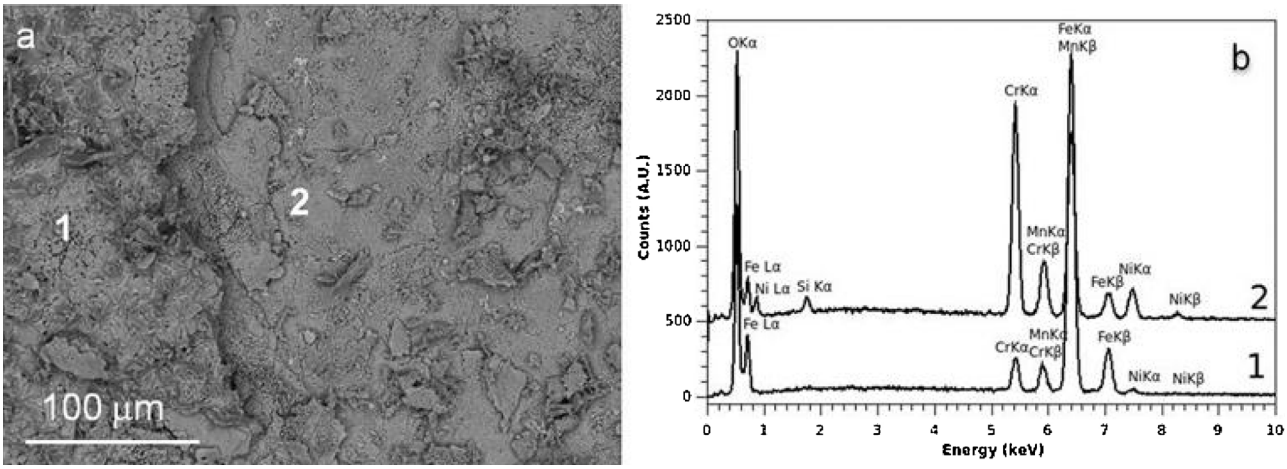

Fig. 3. Surface SEM (a) and EDS spectra (b) of oxide scale isothermally grown on AISI 303 for 50 h at 1000 °C under synthetic air: (1) refers to an unspalled area (2) refers to a spalled area.

and 2.6×10^{-5} mg^2/cm^4/s for the AISI 303 alloy while it was between 1.6×10^{-6} and 6.6×10^{-6} mg^2/cm^4/s for the AISI 304L alloy. Visual observation of samples after 50 h at 1000 °C and cooling also showed a large extent of spallation on the AISI 303 sample, but almost none on AISI 304L. This fact was confirmed by TGA data for AISI 303, for which a significant weight loss was observed during cooling after buoyancy correction [9]. SEM surface view and local EDS spectra of the oxide scale isothermally grown on AISI 303 for 50 h at 1000 °C under synthetic air are displayed in Fig. 3. Two zones were studied: zone (1) corresponds to an unspalled area and zone (2) corresponds to a spalled area. On the EDS spectra, an oxygen peak is clearly identified in the spalled area, indicating that spallation during cooling occurs inside the oxide scale.

The morphology of the oxide scales has been fully described in a companion paper [9], here, we only present results relevant for the understanding of oxide scale mechanical and thermal cycling behavior.

Representative cross-sections of the oxide scales formed on the surface of AISI 304L and AISI 303 alloys after 50 h isothermal oxidation at 1000 °C are displayed in Fig. 4a, b. After 50 h at 1000 °C, AISI 304 L steel presents a continuous and protective oxide layer whereas breakaway oxidation happens for AISI 303 steel with a thicker oxide scale and the formation of oxide gulfs, growing inward (10–15 µm deep into the metal), mainly composed of alternated Fe-rich and Cr-rich oxide layers. The oxide scale on the AISI 303 steel contains more Fe and is more porous than the one on the AISI 304L steel. According to Raman spectroscopy, chromia Cr_2O_3 and solid solution $(Fe,Cr)_2O_3$ as well as spinel $MnCr_2O_4$ are present in the scale grown on AISI 304L. For AISI 303, different spectra were recorded depending on the analyzed zone: Fe-rich spinel type oxide $(Fe,Cr)_3O_4$ for the spalled region and Fe-rich corundum type oxide Fe_2O_3 and $(Fe,Cr)_2O_3$ for the unspalled region.

Moreover, in the AISI 304L steel, internal oxidation of Si can be observed at the metal/oxide interface and along grain boundaries in the metal to a depth of about 10 µm. From SEM cross sectioned views, the density of SiO_2 intrusion along the grain boundaries was evaluated to 42 ± 3 mm^{-1}. In the case of the AISI 303 specimen, SiO_2 is also present in the area where the oxide grew inside the metal: SiO_2 thin films can be distinguished between the layers. Oxidation of Si at the metal/oxide interface or inside the metal matrix has been already reported in the literature [22–24]. SiO_2 is a stable oxide at those high temperatures and for this composition and Si oxidation is possible due to the diffusion of oxygen inside the metal matrix, particularly along the SiO_2/metal boundaries and due to the diffusion of Si in the metal towards the tip of the SiO_2 intrusions. Grain boundaries being short cut path for diffusion, the SiO_2 intrusions along grain boundaries grow to a greater depth there than inside the grains.

In the metal, some phase changes are also observed after isothermal oxidation. The presence of a BCC phase after oxidation of austenitic stainless steels has already been reported and its origin has been discussed. It may be attributed to ferrite due to the local composition change of the steel just below the oxide layer [25] or to BCC martensite [26,27].

In the case of AISI 304L steel, chromium depletion occurred at a depth of 10–15 µm and along the grain boundaries of former austenite. EBSD observations (Fig. 4c) shows that about two rows of austenite grains transformed into martensite below the oxide/metal interface. This transformation probably occurred during the cooling to room temperature and may be due to depletion in Cr but also Mn and Si. Indeed, martensite formation in austenitic stainless steel has already been observed and attributed to an increase of the Ms temperature due to the depletion in some elements like Cr or Mn [26,27]. In the AISI 303 steel, austenite to martensite transformation can also be observed but to a lesser extent than in the AISI 304L (Fig. 4d). In the first row of grains under the oxide/metal interface only some martensite laths are observed within the austenite grains.

Consequently, even if AISI 303 and AISI 304L have similar chemical compositions, except for the S content, their oxidation behavior differ. While AISI 304L still exhibits a fairly protective oxide scale after 50 h at 1000 °C, AISI 303 presents a catastrophic behavior characterized by a high oxidation rate and spallation. Breakaway oxidation of AISI 303 has been previously explained by a mechanism involving the MnS precipitates close to the metal/oxide interface [9].

3.2. Mechanical testing

In situ SEM tensile tests were driven on the isothermally oxidized steels (50 h at 1000 °C). The two stainless steels exhibit similar stress–strain curves (see Fig. 5) even if the AISI 303 steel seems to have a slightly higher hardening rate. Nevertheless, the behavior of the oxide layers were quite different (see Fig. 6). While we observed transverse crack initiation and growth in the oxide scale for both steels, the crack patterns were different. In both cases the cracks grew perpendicular to the tensile direction, but while cracks in the oxide scale of the AISI 303 steel propagated straightly (Fig. 6b), the ones in the AISI 304L steel looked like waves (Fig. 6c). During the in situ SEM tensile tests, cracks are observed earlier in

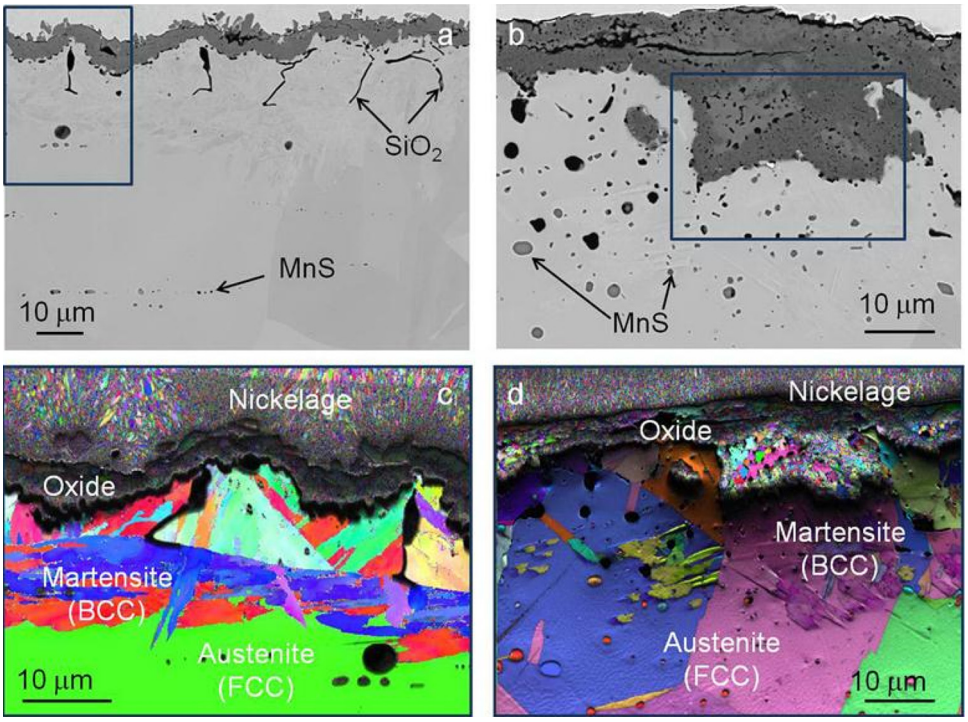

Fig. 4. Representative cross-sections (transversal axis of the samples) of the oxide scales formed on the surface after 50 h isothermal oxidation at 1000 °C under flowing synthetic air and EBSD map of crystallographic orientation of the oxidized steels AISI 304L (a, c), AISI 303 (b, d).

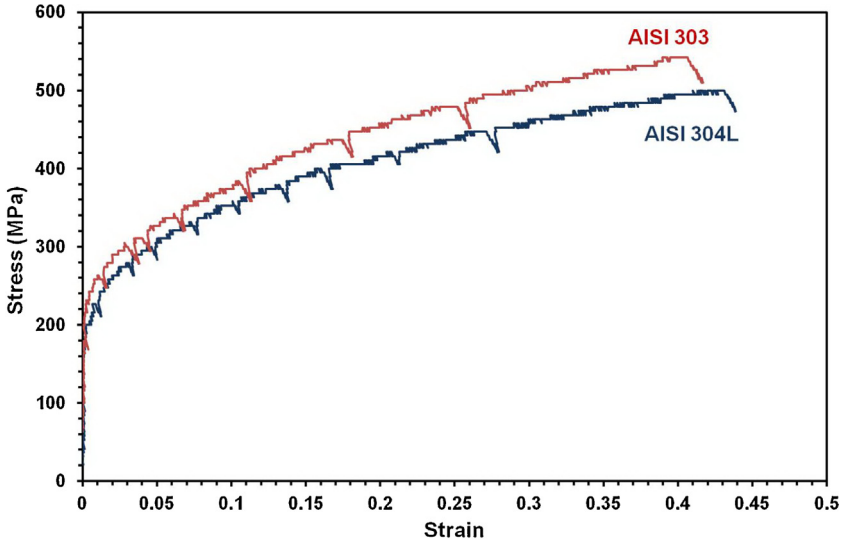

Fig. 5. Stress-strain curves of AISI 303 and AISI 304L steels obtained during tensile tes.

terms of strain on the AISI 303 surface (at about 1.6% strain) than on the AISI 304L one (about 3.4% strain).

Spallation occurs in the oxide scale in the AISI 303 steel (Fig. 6d), but not in the AISI 304L steel. Fig. 6d, f shows that spallation occurred near the metal–oxide interface since the bare metal (bright points) can be distinguished on the surface. Nevertheless, some oxide remains on the fracture surface. It might be the oxide gulfs penetrating in the metal (Fig. 4b) that are entrapped. Crack propagation was easier across those gulfs than it was through the interface around them. In the AISI 304L steel, instead of oxide scale spallation, the transverse cracks opened due to the ductile deformation of the underneath substrate. At the end of the test, when the cracks were wide enough, bare metal could be seen at its root (Fig. 6e).

In order to quantify the damage of the oxide layers, the crack density was measured using the intercept method. A line of a given length is digitally superimposed over the image parallel to the tensile direction. Intercepts are counted every time a crack intercepts with the line. Then the density is simply obtained by dividing the counts by the line length. 5 lines per image were performed and the average density was calculated. The results are reported in Fig. 7 where the evolution of the crack density as a function of longitudinal strain is plotted. In both steels, the crack density increased during the tensile loading till reaching a saturation value. Such a behavior has been already observed in brittle thin films for a more ductile substrate [17,28,29]. For the AISI 303 sample, the saturation part of the curve is not complete because the important spallation of the oxide scale makes the crack density difficult to measure for

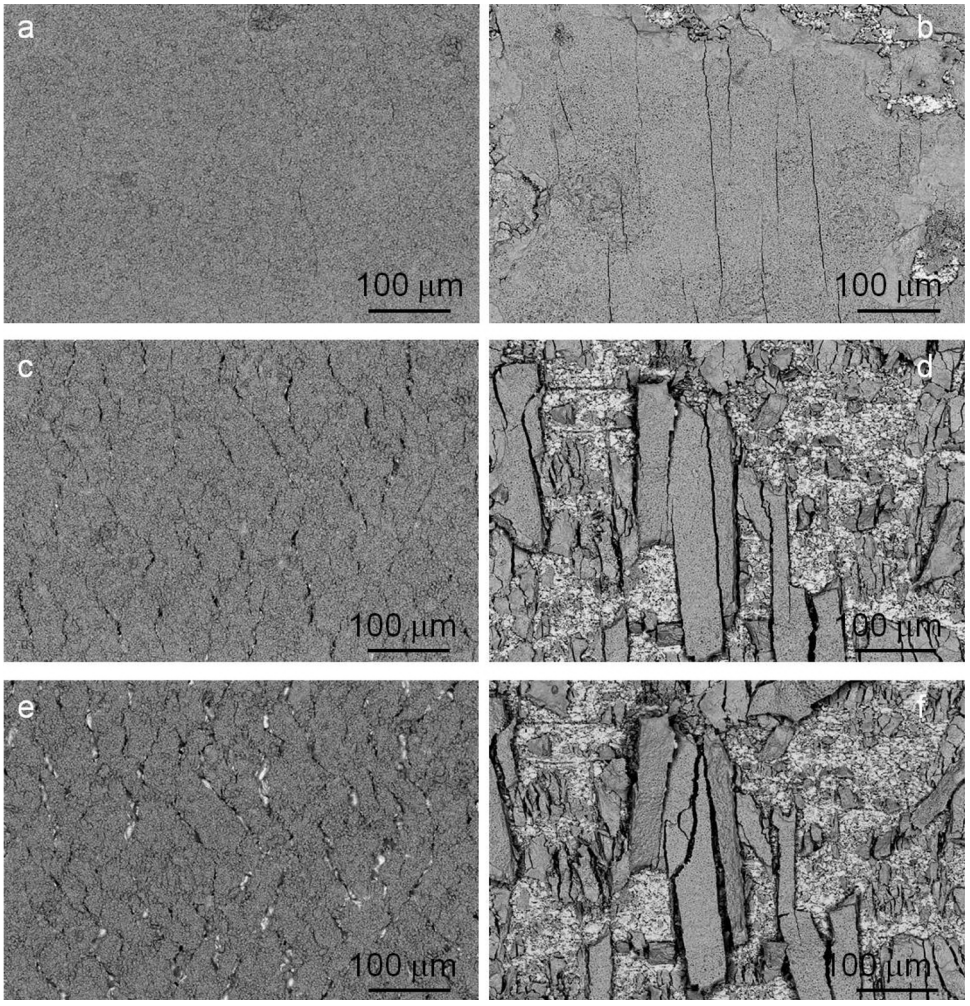

Fig. 6. Surface observations (SEM, back-scattered electron mode) of the oxide scale during tensile test of AISI 304L (a, c, e) and AISI 303 (b, d, f) stainless steel oxidized 50 h at 1000 °C (horizontal = tensile direction): (a) AISI 304L—3.4% strain; (b) AISI 303—1.6 % strain; (c) AISI 304L—17% strain; (d) AISI 303—17% strain; (e) AISI 304L—43% strain (end of test); (f) AISI 303—41% strain (end of test).

larger strain values. But we can notice that the cracking of the oxide scale of the AISI 303 steel is more severe: cracking begins earlier during the tension test, crack density increases faster and the saturation value is higher than for the AISI 304L steel. The evolution of the crack density as a function of the longitudinal strain can be fitted with an empirical expression [17]:

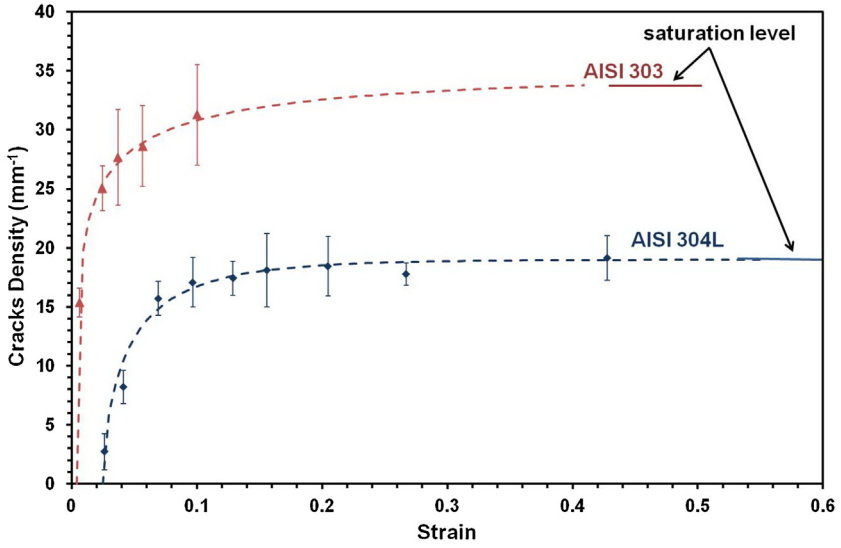

Fig. 7. Crack density evolution during in situ tensile test.

Table 2
Crack density evolution law parameters.

Steel	ϵ_c	d_{sat} (mm^{-1})	n	A
AISI 304L	0.025	19	0.64	11
AISI 303	0.004	35	0.32	4.5

$d(\epsilon) = d_{sat}\left\{1 - \exp[-A(\epsilon - \epsilon_c)^n]\right\}$ (1)where d_{sat} is the crack density at saturation, ϵ_c the critical strain for the cracking of the film, and A and n are constants. d_{sat} is determined by experimental measurement. ϵ_c is obtained by an extrapolation at $d = 0$. A and n are obtained by fitting the linear plot of $\ln(-\ln(1 - d/d_{sat}))$ as a function of $\ln(\epsilon - \epsilon_c)$. The parameters obtained for the two samples are given in Table 2. Those parameters reflect what can be observed on the graph and confirm a more brittle behavior of the AISI 303 oxide scale: lower critical strain for crack initiation ϵ_c and higher saturation density of cracks d_{sat}. The values for the n exponent found here are similar to the ones obtained in a previous work on passivation films deposited on an aluminum substrate [17].

So, both oxide scales exhibit a similar cracking behavior composed of three stages: crack initiation, increase in crack density and finally saturation, i.e. strain without additional cracks. Nevertheless, cracking mechanisms are different for each steel. For AISI 304L, crack initiation appears more difficult and happens for a higher strain value. From cross-section observations after tensile testing (Fig. 8a), the transverse cracks in the oxide layer can be linked to grain boundaries in the metal underneath. So in this case, the cracks may initiate at the metal/oxide interface, facing grain boundaries. Those grain boundaries are themselves embrittled by the growth of SiO_2 oxides. If the cracks grow from the interface up to the surface, this explains their wavy-shape because they follow the morphology of the grain boundaries underneath. In the AISI 303 specimen, the cracks initiate for a lower strain value and most probably from internal flaws in the porous Fe-rich oxide. The cross section in Fig. 8b shows that grain boundaries in the metal also opened during the tensile test, however, here, transverse cracks in the oxide scale grew not only facing these opened grain boundaries but also between them. Finally, in AISI 303 the porosity of the oxide scale also eases the cracks' growth, they can therefore propagate in straight lines, perpendicular to the tensile direction.

Saturation mechanisms also are different in the two steels. In the AISI 303, the crack density saturates at the onset of the oxide scale spallation. In the 304L no spallation occurs. Nevertheless, at some point, localized plastic deformation of the metal at the crack root happens, diminishing the strain transferred to the oxide film. As a result, there is not enough available energy for new cracks to initiate [30]. Those results confirm that the Cr-rich thinner oxide scale thermally grown on AISI 304L is more protective, since it is more resistant and more adherent to the metal than the oxide scale grown on AISI 303. This is consistent with observations on the behavior of the two steels during isothermal oxidation and can be linked to their difference in S concentration. The higher S content in the 303 steel induces MnS precipitates in the metal with a higher density and larger size than in the 304L steel. During the oxidation treatment, MnS precipitates located near the metal/oxide interface oxidize into Mn, Cr rich oxysulfides thus leading to a local depletion in Cr that promotes breakaway oxidation in 303 steel [9].

3.3. Cyclic oxidation

A detailed analysis of cyclic thermogravimetry data of both steels was carried out to compare it with damaging behavior of oxide scales during tensile tests of isothermally pre-oxidized specimens.

The Net Mass Change (M^{NMC}), i.e. the mass change of the sample with its adherent oxide scale but without the spalled oxides, as a function of the number of cycles for AISI 303 and AISI 304L samples are compared in Fig. 9. Oxidation kinetics data includes the mass gain due to oxidation (uptake of oxygen) and the mass loss due to spalling (loss of oxide). Results show the similar cyclic oxidation behavior of the two steels. Indeed, the general shape of the curves is identical. Nevertheless, for AISI 303 steel, the initial oxidation rate was higher and spallation events began earlier than for AISI 304L. The cyclic oxidation behavior revealed the expected improvement in scale retention as the S content decreased. After 55 cycles, the AISI 303 alloy sample underwent significant oxide spallation and drastic loss of oxide scale after 73 cycles, whereas the same phenomena both occurred at 110 cycles for the AISI 304L alloy. The lifetime is approximatively doubled between AISI 303 and AISI 304L. It can also be seen that the breakdown of the oxide scale occurs for a higher M^{NMC} for alloy AISI 304L, which means that AISI 304L is able to retain a thicker oxide scale than alloy AISI 303.

A second observation is that the oxidation kinetics are not parabolic for both alloys. For alloy AISI 304L, the initial M^{NMC}shape is apparently parabolic up to 15 or 20 cycles before becoming linear. For alloy AISI 303, apparent linear kinetics is found after only a few cycles.

Cyclic Thermogravimetry Analysis (CTGA) [20] allows to calculate other characteristical values of the cyclic oxidation kinetics, based on the continuous measurement of the net mass change M^{NMC}. The gross mass gain (M^{GMG}—i.e. the mass variation of the oxidized sample plus the mass of the spalled oxide), the average oxide scale thickness (e_n), and the average thickness of the metal consumed can be calculated as a function of the number of cycles"n".

By definition, the net mass change per unit area of sample surface is simply the measure of the mass variation given by the thermobalance. To measure two phenomena, i.e. the mass gain due to oxidation and mass loss due to oxide spallation, two mass values are necessary for each cycle. It was chosen to name the data at the beginning of the high-temperature dwell n, $M_n{}^{bg}$, and at the end of the high-temperature dwell n, $M_n{}^{end}$. These two masses are measured at the same temperature, therefore there is no variation of buoyancy between them. The net mass change at cycle n, M^{NMC}, can be simply defined as:

$$M_n^{NMC} = M_n^{end} \tag{2}$$

The gross mass gain can be calculated using the two M^{NMC}values recorded for each cycle. If we neglect the oxidation during heating and cooling, the gross mass gain per unit area of sample surface at the end of cycle n $M_n^{GMG}$is simply the sum of all mass gain during high temperature dwells:

$$M_n^{GMG} = \sum_{j=1}^{n}\left(M_j^{end} - M_j^{bg}\right) \tag{3}$$

The evaluation of the average thickness of the oxide scale after n cycles, e_n, can be done through the determination of the mass of the adherent oxide scale per unit area of sample surface (M_n^{AOX}):

$$M_n^{AOX} = M_{n+1}^{bg} + \left(\frac{1}{r} - 1\right)\sum_{j=1}^{n}\left(M_j^{end} - M_j^{bg}\right) - M_1^{bg} \tag{4}$$

where r is the ratio between the mass of oxygen in the oxide and the mass of the oxide. When the mass gain due to oxidation during heating and cooling cannot be neglected compared to the mass gain during the high temperature dwell, it is necessary to take into account the buoyancy effect during the temperature transients [31].

The average oxide scale thickness is given by:

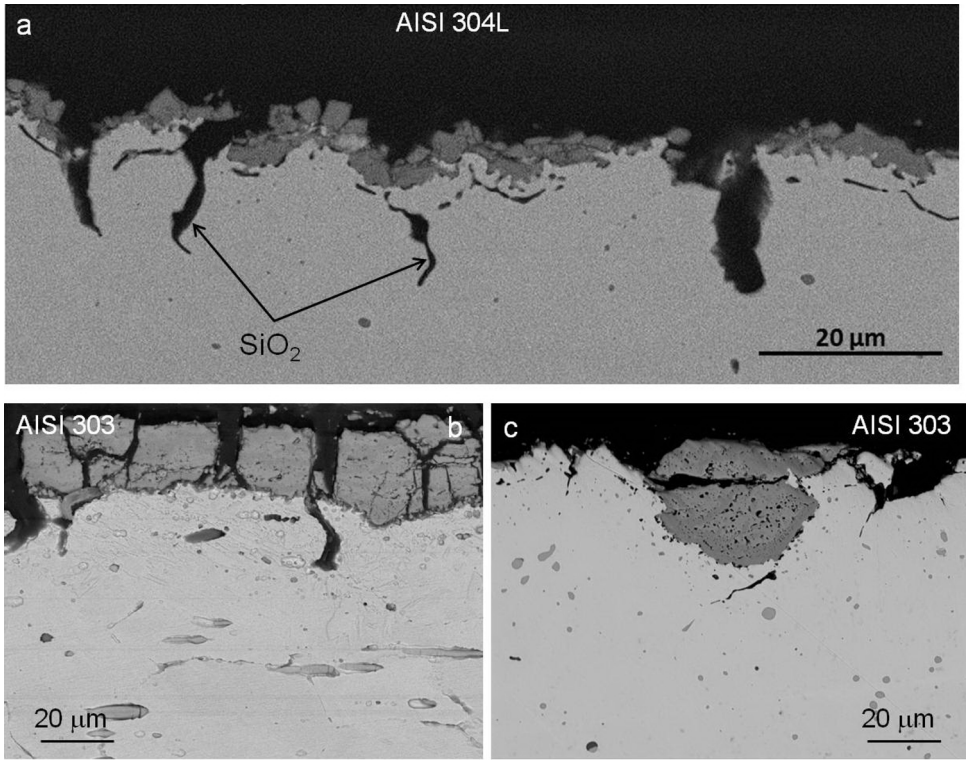

Fig. 8. Micrographs of the steels after isothermal oxidation 50 h at 1000 °C and tensile testing: AISI 304 L transverse axis of the sample (a); AISI 303 cross-section along longitudinal axis of the sample (b); AISI 303 cross-section along transverse axis of the sample (c).

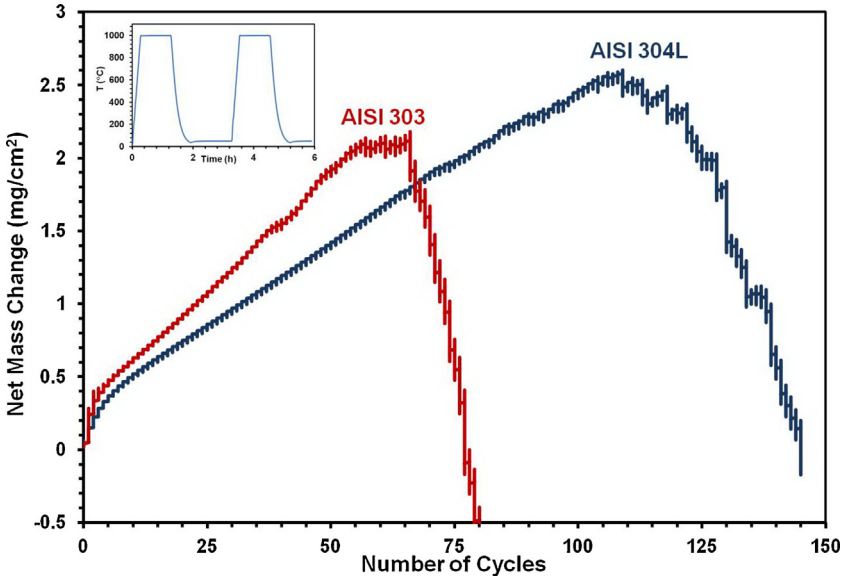

Fig. 9. Cyclic oxidation behavior of AISI 303 and AISI 304L samples at 1000 °C and thermal profile of the first two cycles.

$e_n = \frac{M_n^{AOX}}{\rho}$ (5)where ρ is the density of the oxide. Assuming that the oxide scale is mainly Cr_2O_3, $\rho = 5.2\ g/cm^3$.

The resulting values for AISI 303 and AISI 304L are plotted in Fig. 10 as a function of the number of cycles. The oxidation during the non-isothermal periods was neglected compared to the oxidation during the high temperature dwell. This approximation leads to a small error, as can be seen in Fig. 10b (AISI 304L), where the gross mass gain and the net mass change curves cross while the gross mass gain should be equal to the net mass change in the absence of spallation and higher than the net mass change when spallation occurs. This shows that the gross mass gain is slightly under-evaluated, especially for alloy AISI 304L which exhibits more oxidation during heating than AISI 303 (Fig. 10a), and the same observation can be made for the evaluation of the average thickness of the oxide scale.

Despite this slight approximation, it can be clearly seen from the graphs that the oxide scale thickness increases almost linearly after about 5 cycles for AISI 303 and after 20 cycles for AISI 304L. Breakaway occurred at 5 and 20 cycles respectively, meaning that the oxide scale does not offer a good diffusion barrier and that oxidation kinetics is controlled by the reaction rate. The average oxide scale

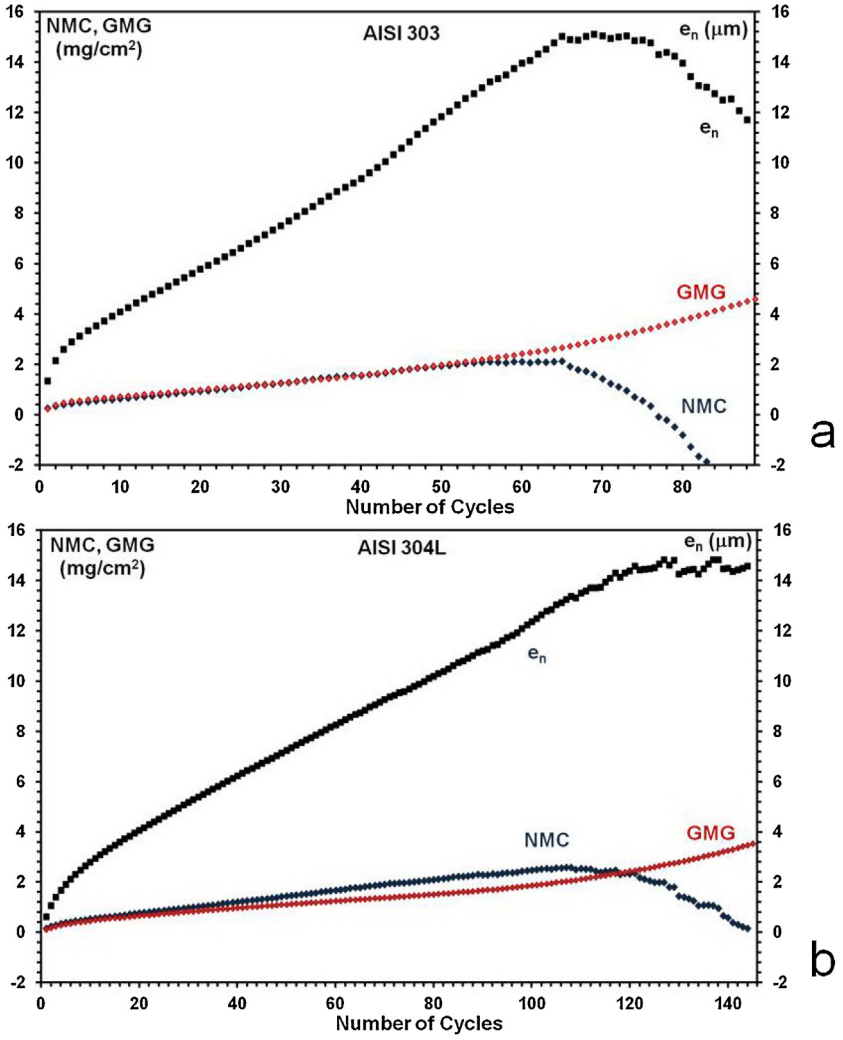

Fig. 10. Net Mass Change (NMC), Gross Mass Gain (GMG) and average oxide scale thickness (e_n) for AISI 303 (a) and AISI 304L (b) using thermogravimetry during thermal cycling at 1000 °C.

thickness continues to grow up to about 15 μm (certainly slightly more for AISI 304L due to the approximation) where it becomes constant. The oxidation regime with a constant average oxide scale thickness corresponds to the stationary kinetics resulting from the compensated effects of oxidation and spallation during each cycle [20]. After 73 cycles, a complete breakdown of the oxide scale for alloy AISI 303 is observed.

In order to understand the effects of thermal cycling, results were compared with those obtained from isothermal tests. The net mass change curves obtained during 50 h and 150 h for isothermal oxidation of AISI 304L samples at 1000 °C and for 145 cycles of 1 h at 1000 °C under synthetic air flow for the same flow rate are presented in Fig. 11.

Despite some dispersion of isothermal oxidation results, especially during the initial transient regime, it is clear that the net mass change curve obtained during cyclic oxidation shows faster oxidation kinetics after the transient regime and up to 70 h. The fact that the oxidation rate increases without any mass loss, indicates that the oxide scale has been fractured without spalling, and that during temperature transients, re-oxidation heals these cracks. This will be discussed more thoroughly in a coming paper.

At this stage, we can propose a first understanding of the effect of thermal cycling on the oxidation kinetics. During isothermal oxidation, a first stage of faster kinetics is observed before reaching a protective parabolic behavior after 10–15 h (Fig. 11). During thermal cycling, the same thing occurs at the beginning, but a few cycles after the establishment of an oxygen diffusion barrier of a few micrometers thick oxide (Fig. 10), fractures of the scale occur during cooling inducing an enhanced re-oxidation during next heating cycle and high temperature dwell. This causes the overall oxidation kinetics to increase from a parabolic law to a linear law. The oxide scale becomes thicker than for isothermal kinetics and such enhanced oxidation kinetics eventually leads to the spalling of the oxide scale. Spalling during isothermal oxidation does not occur because of the absence of thermal stresses and because the oxide scale is thinner than for thermal cycling. Nevertheless, as reported in our previous paper [9], some spalling occurs during the final stage of cooling of the 50 h isothermal experiment.

To determine the nature of the phases present in the scales after cyclic oxidation, the surfaces and the cross-sections of specimens of both alloys were characterized using SEM-EDS. These analyses were carried out after 89 (AISI 303) and 145 (AISI 304L) cycles, after the breakdown of the protective oxide scale as shown previously. Cross-section analysis (Fig. 12) shows that the interface between oxide and metal is very rough. Nevertheless, the observation is consistent with the calculated average scale thickness of 15 μm before breakdown (calculated from the total amount of oxide in relation to the surface area of the sample).

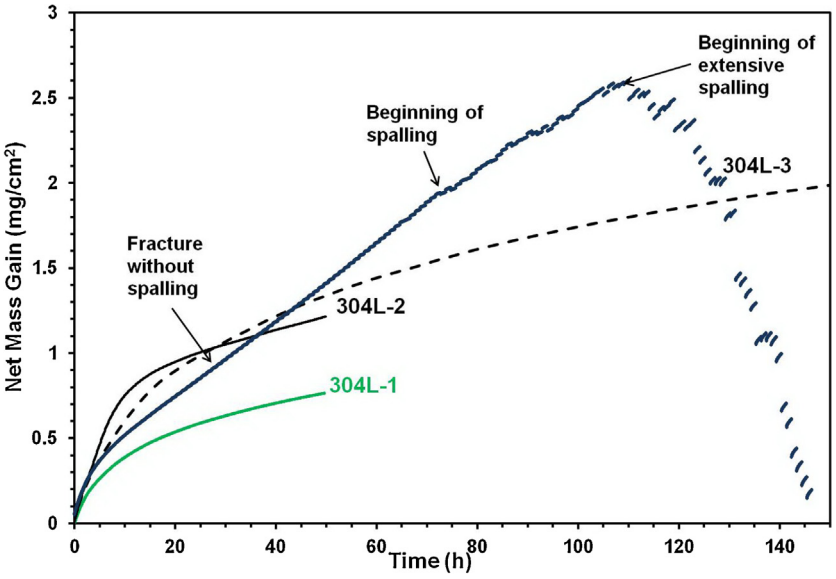

Fig. 11. Net Mass Change of AISI 304 L samples oxidized during 50 h (304 L-1, 2) and 150 h (304L-3) in isothermal condition at 1000 °C and during 145 cycles of 1 h at 1000 °C under synthetic air flow for the same flow rate. Mass gain during heating and cooling is not included.

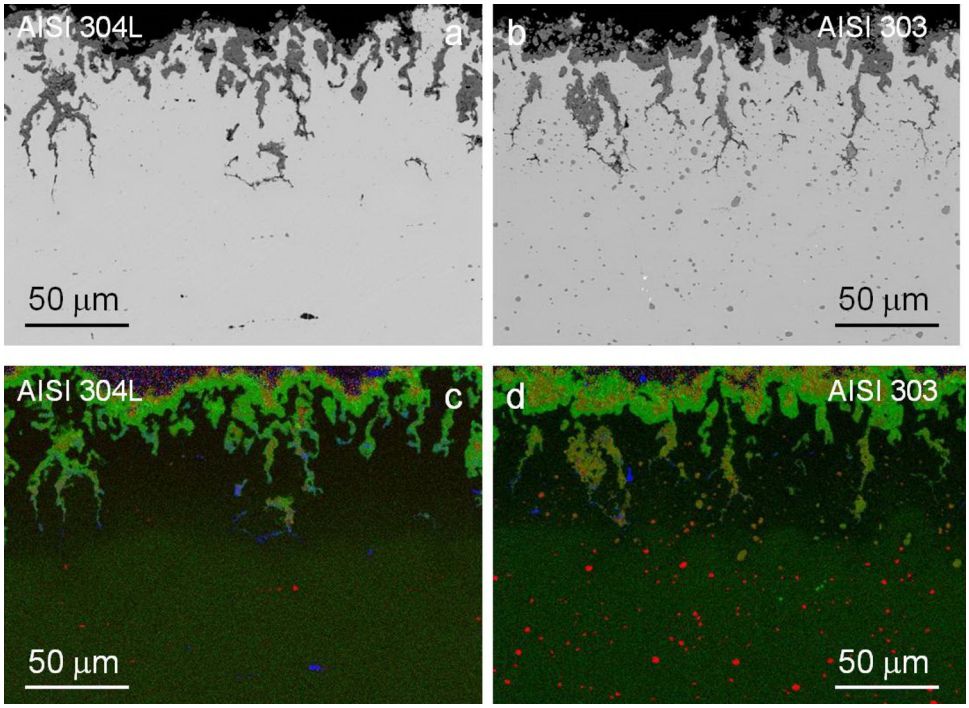

Fig. 12. SEM cross-sections of AISI 304L (a) and AISI 303 (b) steels after cyclic oxidation at 1000 °C in air (after 145 and 89 cycles respectively) and EDS maps of AISI 304L (c), AISI 303 (d): Cr Kα in green, Mn Kα in red, Mn + Cr in orange, Si Kα in blue. For interpretation of the references to colour in this figure legend, the reader is referred to the web version of this article.

According to Fig. 12, the internal part of the oxide layer (green in Fig. 12c, d) is a Cr-rich oxide. The external part of the oxide is Mn-rich (light orange in Fig. 12c, d), probably the spinel type oxide $(Mn,Fe)Cr_2O_4$. The formation of internal more stable oxide, SiO_2, was observed along the grain boundaries in the substrate and below the duplex oxide scale (Si is blue in Fig. 12c, d).

The EDS-maps confirm the larger quantity of MnS precipitates for AISI 303 alloy in comparison with AISI 304L. The increase in number and decrease in size of the S containing precipitates close to the metal/oxide interface was also observed for AISI 303 (Fig. 12d).

XRD analyses were performed to identify the phases present on the surface of the oxide scale after cyclic oxidation (Fig. 13). The XRD analysis of the two oxidized steels showed the presence of Cr_2O_3 and $(Mn,Fe)Cr_2O_4$ spinel in the oxide layers. FCC and BCC Fe-rich phase related to the metallic substrate were also detected. The presence of the BCC phase is related to martensite transformation.

During thermal cycling it seems that the cracks appear and follow the brittle silica intrusions along the grain boundaries in a zone of martensite transformation (Fig. 14). This transformation occurred under the oxide layer in a Cr depleted zone due to selec-

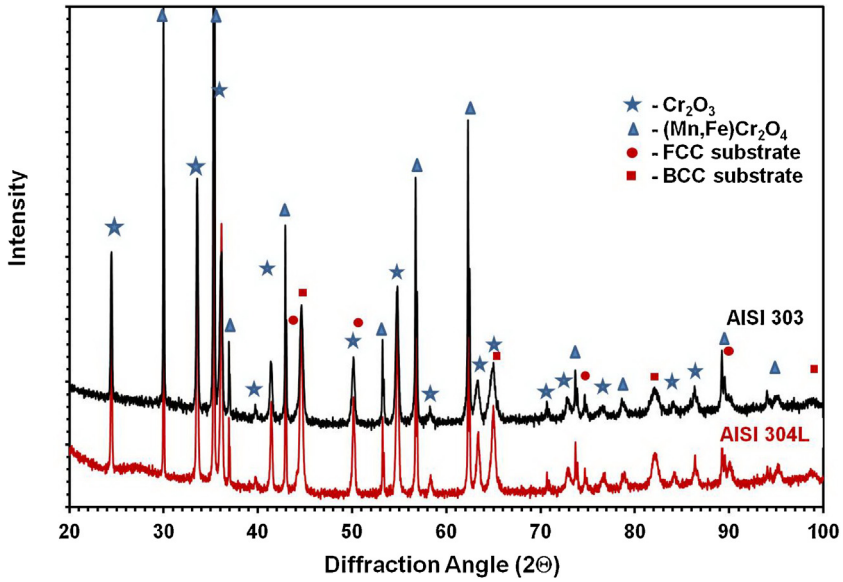

Fig. 13. XRD analyses of AISI 304L and AISI 303 steels after cyclic oxidation at 1000 °C in air (after 145 and 89 cycles respectively).

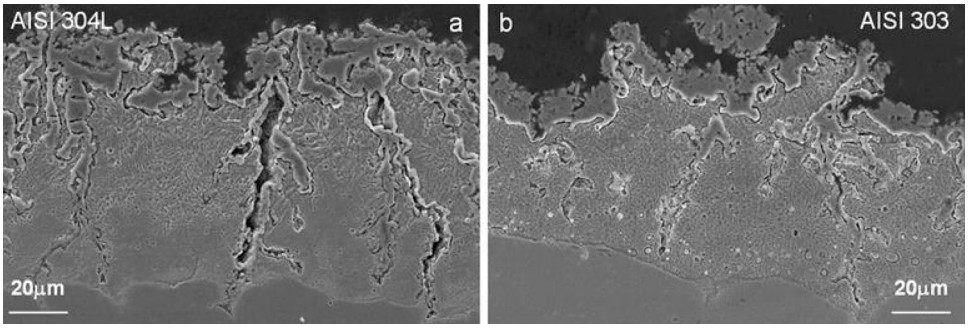

Fig. 14. SEM cross-sections of AISI 304L and AISI 303 (b) steels after cyclic oxidation at 1000 °C in air (after 145 and 89 cycles correspondently) and chemical etching.

tive oxidation which was observed to a depth of about 60 μm (Figs. 12 c, d, 14).

Therefore, similar to what was observed for tensile test results, the oxide scale behavior during the cyclic oxidation of both steels can be divided into three stages. During the first stage the net mass change shape is parabolic up to the 20th cycle for AISI 304L and about the 5th cycle for AISI 303. This stage corresponds to oxidation without cracking and establishment of an oxide diffusion barrier of a few micrometers thick.

During the second stage, the oxidation kinetic changes from a parabolic law to a linear law. The interpretation of this result appears to be embrittlement and crack formation in the metal grain boundaries due to significant tensile thermal stress in the metal during cooling. Consequently, enhanced oxidation has been observed during the following heating and high temperature dwell. Creep relaxation occurs at 1000 °C and continues a little bit during cooling while the oxide is under compression and the metal under tension due to thermal expansion mismatch between the oxide scale and the substrate. When this occurs, at the end of the next heating, the oxidized grain boundary is under tension and may crack and open. This crack can propagate into the external oxide scale which is also in tension during heating. Moreover, the presence of silica at grain boundaries in the substrate, with a huge thermal expansion mismatch with the alloy ($0.5–1 \times 10^{-6}\,°C^{-1}$ for SiO_2 and $13–15 \times 10^{-6}\,°C^{-1}$ for the alloy), leads to intergranular crack tips being under tension at the beginning of the heating because of a leverage effect. This mechanism is more obvious for the AISI 304L alloy which is characterized by a large branched zone of internal Si oxidation (Fig. 14). This is explained by the fact that the external oxide scale is more resistant on alloy AISI 304L which leads to a higher stress level in the substrate. For AISI 303, the external scale presents more cracks causing a lower level of thermal stress in the metallic substrate.

During the third stage, a significant oxide spallation followed by a drastic loss of the oxide scale was observed for both steels, but the lifetime was approximately twice as much for AISI 304L than for AISI 303. This is the consequence of the kinetics of cyclic oxidation observed in the second stage. It may also be accelerated by a chemical breakaway observed sooner for alloy 303 than for alloy 304L. Indeed, in a companion paper, it was proposed that breakaway oxidation of AISI 303 was related with the presence of numerous oxysulfide inclusions close to the metal/oxide interface [9]. This explanation should be valid for the cyclic oxidation as well, leading to enhanced oxidation kinetics and poor mechanical properties of the oxide scale and therefore to the large and fast decrease in net mass change (M_n^{NMC}).

4. Conclusions

1. The oxide scale formed on the high S content AISI 303 steel is less protective than the one on the AISI 304L steel. Both CTGA and tensile tests show that the oxide scale cracks sooner on AISI 303. This corresponds to faster cyclic oxidation kinetics for AISI 303 and to a final catastrophic spallation of the oxide scale.

2. The weaker resistance of the oxide scale formed on AISI 303 stainless steel is proposed to be due to its higher S content, through an indirect mechanism involving Cr trapping in Cr–Mn rich oxysulfides which eventually leads to an Fe-rich oxide scale with breakaway oxidation.
3. SiO_2 intrusions are observed along the alloy grain boundaries which weaken them and facilitate crack initiation in both the metal and the oxide scale during thermal cycling.

Acknowledgements

The authors gratefully acknowledge Pierre Chemelle (Ugine), Natalia Nikolaeva (SibFU) and Yannick Thebault (CIRIMAT) for their help with electron microscopy observations.

This work was realized in the framework of a PICS project supported by the National Centre for Scientific Research (CNRS, France) Ref no 6095 and the Russian Foundation for Basic Research (RFBR, Russia) Ref no 13-08-91053-CNRS_a.

References

[1] A.W. Funkenbusch, J.G. Smeggil, N.S. Bornstein, Reactive element–sulfur interaction and oxide scale adherence, Metall. Trans. A 16A (1985) 1164–1166.
[2] G. Smeggil, A.W. Funkenbusch, N.S. Bornstein, A relationship between indigenous impurity elements and protective oxide scale adherence characteristics, Metall. Trans. A 17A (1986) 923–932.
[3] J.L. Smialek, Adherent Al_2O_3 scales formed on undoped NiCrAl alloys, Metall. Trans. A 18A (1987) 164–167.
[4] P.Y. Hou, J. Stringer, Oxide scale adhesion and impurity segregation at the scale/metal interface, Oxid. Met. 38 (1992) 323–345.
[5] T. Gheno, D. Monceau, D. Oquab, Y. Cadoret, Characterization of sulfur distribution in Ni-based superalloy and thermal barrier coating after high temperature oxidation: a SIMS analysis, Oxid. Met. 73 (2010) 95–113.
[6] H.J. Grabke, D. Wiemer, H. Viefhaus, Segregation of sulfur during growth of oxide scales, Appl. Surf. Sci. 47 (1991) 243–250.
[7] V.K. Tolpygo, H. Viefhaus, Segregation at the Al_2O_3–FeCrAl interface during high-temperature oxidation, Oxid. Met. 52 (1999) 1–29.
[8] D. Lees, On the reasons for the effects of dispersions of stable oxides and additions of reactive elements on the adhesion and growth-mechanisms of chromia and alumina scales—the sulfur effect, Oxid. Met. 27 (1987) 75–81.
[9] C. Pascal, V. Parry, E. Fedorova, M. Braccini, P. Chemelle, N. Meyer, D. Oquab, D. Monceau, Y. Wouters, M. Mantel, Breakaway oxidation of austenitic stainless steels induced by alloyed sulphur, Corros. Sci. 93 (2015) 100–108.
[10] M.D. Drory, J.W. Hutchinson, Measurement of the adhesion of a brittle film on a ductile substrate by indentation, Proc. R. Soc. Lond. 452 (1996) 2319–2341.
[11] S.J. Bull, Failure mode maps in the thin film scratch adhesion test, Tribol. Int. 30 (1997) 491–498.
[12] S.J. Bull, E.G. Berasetegui, An overview of the potential of quantitative coating adhesion measurement by scratch testing, Tribol. Int. 39 (2006) 99–114.
[13] F. Attar, T. Johannesson, Adhesion evaluation of thin ceramic coatings on tool steel using the scratch testing technique, Surf. Coat. Technol. 78 (1996) 87–102.
[14] I. Hofinger, M. Oechsner, H.A. Bahr, M.V. Swain, Modified four-point bending specimen for determining the interface fracture energy for thin, brittle layers, Int. J. Fract. 92 (1998) 213–220.
[15] M.N. Nagl, W.T. Evans, D.J. Hall, S.R.J. Saunders, An in situ investigation of the tensile failure of oxide scales, Oxid. Met. 42 (1994) 431–449.
[16] S. Chandra-Ambhorn, F. Roussel-Dherbey, F. Toscan, Y. Wouters, A. Galerie, M. Dupeux, Determination of mechanical adhesion energy of thermal oxide scales on AISI 430Ti alloy using tensile test, Mater. Sci. Technol. 23 (2007) 497–501.
[17] P. Scafidi, M. Ignat, Cracking and loss of adhesion of Si_3N_4 and SiO_2: P films deposited on Al substrates, J. Adhes. Sci. Technol. 12 (1998) 1219–1242.
[18] M.S. Hu, A.G. Evans, The cracking and decohesion of thin films on ductile substrates, Acta Metall. 37 (1989) 917–925.
[19] E. Fedorova, D. Monceau, D. Oquab, Quantification of growth kinetics and adherence of oxide scales formed on Ni-based superalloys at high temperature, Corros. Sci. 52 (2010) 3932–3942.
[20] D. Monceau, D. Poquillon, Continuous thermogravimetry under cyclic conditions, Oxid. Met. 61 (2004) 143–163.
[21] D. Monceau, B. Pieraggi, Determination of parabolic rate constants from a local analysis of mass–gain curves, Oxid. Met. 50 (1998) 477–493.
[22] R.K. Wild, High temperature oxidation of austenitic stainless steel in low oxygen pressure, Corros. Sci. 17 (1977) 87–104.
[23] G.J. Yurek, D. Eisen, A. Garratt-Reed, Oxidation behavior of fine-grained rapidly solidified 18-8 stainless steel, Metall. Trans. A 13A (1982) 473–485.
[24] S.N. Basu, G.J. Yurek, Effect of alloy grain size and silicon content on the oxidation of austenitic Fe–Cr–Ni–Mn–Si alloys in pure O_2, Oxid. Met. 36 (1991) 281–315.
[25] D. Lussana, D. Baldissin, M. Massazza, M. Baricco, Thermodynamic and kinetics aspects of high temperature oxidation on a 304L stainless steel, Oxid. Met. 81 (2014) 515–528.
[26] D. Oquab, C. Josse, A. Freulon, Y. Thebeault, C. Charvillat, O. Marsan, J. Esvan, D. Galy, Oxidation and phase transformation of austenitic 304L steel under accidental high temperature condition, in: EUROCORR 2013, 2–5 September Estoril, Portugal, 2013.
[27] A. La Fontaine, H.-W. Yen, P. Trimby, S. Moody, S. Miller, M. Chensee, S. Ringer, J. Cairney, Martensitic transformation in an intergranular corrosion area of austenitic stainless steel during thermal cycling, Corros. Sci. 85 (2014) 1–6.
[28] O. Bernard, G. Amiri, C. Haut, B. Feltz, A.M. Huntz, M. Andrieux, Mechanical and microstructural characterization of oxide films damage, Mater. Sci. Eng. A 335 (2002) 32–42.
[29] A. Galerie, F. Toscan, E. N'Dah, K. Przybylski, Y. Wouters, M. Dupeux, Measuring adhesion of Cr_2O_3 and Al_2O_3 scales on Fe-based alloys, Mater. Sci. Forum 461–464 (2004) 631–638.
[30] H. Rehman, F. Ahmed, C. Schmid, J. Schaufler, K. Durst, Study on the deformation mechanics of hard brittle coatings on ductile substrates using in situ tensile testing and cohesive zone FEM modeling, Surf. Coat. Technol. 207 (2012) 163–169.
[31] A. Raffaitin, D. Monceau, E. Andrieu, F. Crabos, Cyclic oxidation of coated and uncoated single-crystal nickel-based superalloy MC2 analysed by continuous thermogravimetry analysis, Acta Mater. 54 (2006) 4473–4487.